

www.acsanm.org Article

## Silicene/Silicene Oxide Nanosheets for Broadband Photodetectors

Roberto Gonzalez-Rodriguez, Roxana M. del Castillo, Evan Hathaway, Yuankun Lin, Jeffery L. Coffer, and Jingbiao Cui\*



Cite This: ACS Appl. Nano Mater. 2022, 5, 4325-4335



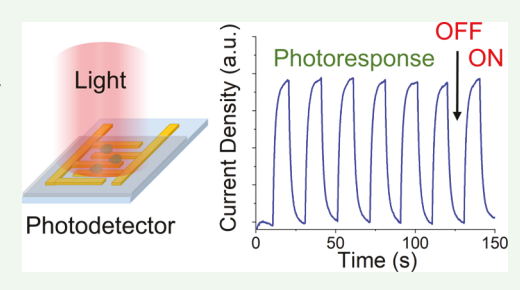
**ACCESS** 

Metrics & More

Article Recommendations

Supporting Information

ABSTRACT: Nanosheets of silicene, a 2D material made of silicon atoms, have great potential for use in next-generation electronic and optoelectronic devices due to their unique properties. However, issues in the large-scale production of silicene nanosheets and in their degradation still present challenges for these applications. Here, we report a method to obtain large quantities of single to fewlayer thick silicene/silicene oxide ("Si nanosheets") from calcium disilicide (CaSi<sub>2</sub>). We also show that the silicene nanosheets experience oxidation in air and are highly oxidized after 12 weeks of storage. Density functional theory studies were performed and provide a detailed understanding of this oxidation. Silicene/ silicene oxide nanosheet-based photodetector devices were also fabricated for the



first time. They show a broadband response in the visible spectral range with outstanding responsivity (14.3 A/W), detectivity (3  $\times$ 10<sup>10</sup> Jones), and external quantum efficiency (44.6%), demonstrating the promising applications of this material for optoelectronic devices.

**KEYWORDS:** silicene, silicene oxide, 2D material, degradation, photodetector, optoelectronics

## 1. INTRODUCTION

Since the discovery of graphene by Novoselov in 2004, 2D materials have attracted much attention from the scientific community, expanding to a diverse range of material systems, such as graphene oxide, 2,3 transition-metal dichalcogenides, germanene,<sup>5</sup> and silicene.<sup>6</sup> In comparison to their bulk counterparts, the 2D form of these materials has outstanding optical and electronic properties along with very large surface areas. These unique properties have potential applications in a wide variety of fields such as photovoltaics,7 battery technology, 8,6 catalysis, 10 and sensing and photodetectors. 11,12

Silicon is a key material in semiconductor technology. The corresponding 2D material of silicon is silicene, similar to the naming convention of graphene as the 2D form of graphite. Silicene lacks planarity with regard to sheet geometry due to the sp<sup>2</sup>/sp<sup>3</sup> mixed hybridization, resulting in a buckled conformation, 13 and is therefore unstable. Silicene can be produced by epitaxial growth on substrates such as Ag(111), Ag(11/0), Ag(001), Ir(111), Au(110), as well as on other surfaces such as ZrBrB<sub>2</sub>. Such growth techniques require very complex and expensive ultrahigh vacuum systems, and the yields are extremely low. 17,20-22 In addition to the small quantity produced by epitaxial methods, hybridization of the substrate (such as Ag or Si) makes it very difficult to modulate the Fermi level in silicene due to the formation of a metallic band caused by hybridization at the interface.<sup>23</sup> As such, silicene synthesis in large quantities is still challenging and presents questions for the scalability of production in the future. Chemical routes offer a solution to this scalability problem. One of the most common methods for the large-scale

production of silicene is the removal of Ca or Mg from exfoliated calcium disilicide (CaSi<sub>2</sub>) or MgSi<sub>2</sub> structures, leaving behind silicene layers 24 There is still inconsistency in the literature regarding the naming of the products formed by the removal of Ca species from CaSi2 using aqueous HCl. These products have been referred to as Wöhler siloxene (H termination on one side of the sheet and OH on another), Kautsky siloxene (Si<sub>6</sub>H<sub>6</sub> rings with oxo bridges), 2D silicon sheets either terminated by H or OH groups, or 2D silicon oxide sheets by various groups.<sup>25</sup>

The interconnected Si<sub>6</sub> rings in silicene layers form hexagonal 2D silicon sheets. Since the silicene layers are very air-sensitive, several methods have been proposed to stabilize them. One of the most common methods is chemical functionalization that stabilizes the silicene surface with organic surface modification reactions such as hydrosilylation, amine-containing condensation reactions, or Grignard reactions (e.g., phenyl magnesium bromide). 24,26 However, this chemical functionalization can dramatically change the optical and electronic properties of silicene. For this reason, we protect the silicene layers with a thin film of Al<sub>2</sub>O<sub>3</sub> deposited

Received: January 21, 2022 Accepted: February 25, 2022 Published: March 8, 2022





by atomic layer deposition (ALD), which has previously been used for the protection of 2D materials.<sup>27</sup>

It is generally accepted in the scientific literature that tunneling heterostructures provide a versatile architecture for photodetection, advanced optical sensitivity, and well-balanced photoelectric performance. Photodetectors based on 2D materials such as graphene, BO, WS<sub>2</sub>, Mo, Te<sub>2</sub>, ZnS, and so on have been reported. Currently, 2D materials for photodetector applications are categorized as either zero, narrow, middle, or wide band gap semiconductors. Due to the unique properties and versatility of silicene, we investigated the performance of a silicene-based photodetector, which is a narrow band gap semiconductor.

In this study, we report on the synthesis of single layer, few layer, and multilayers of silicene and silicene oxides ("Si nanosheets") by calcium removal from CaSi<sub>2</sub> and their applications in broadband photodetectors. We also probed the stability of this material in air and with a 15 nm-thick protective layer of Al<sub>2</sub>O<sub>3</sub> deposited by ALD using Raman spectroscopy. The experimental results were interpreted with assistance from computational simulations. For the first time, we fabricated a broadband (400–808 nm) photodetector based on silicene, which showcases outstanding performance in terms of responsivity, detectivity, and external quantum efficiency, demonstrating the promising potential of silicene/ silicene oxide in optoelectronic devices.

## 2. RESULTS AND DISCUSSION

Silicene/silicene oxide layers were fabricated through the removal of calcium ions from CaSi<sub>2</sub> as shown in Figure 1. The

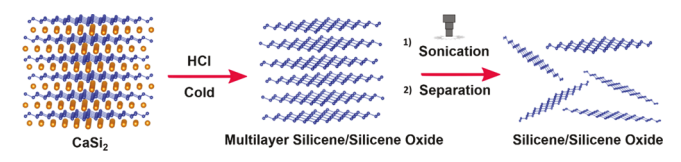


**Figure 1.** Diagram for the fabrication of silicene/silicene oxide layers from CaSi<sub>1</sub>.

starting material, CaSi<sub>2</sub>, was chosen because it has a layered structure with alternating layers of silicon and calcium. The removal of Ca<sup>2+</sup> can be achieved simply by immersing the material in concentrated HCl, which leads to a multilayer (ML) structure.<sup>30,31</sup> A sonication process followed by centrifugation is necessary to obtain a single layer or few layers of silicene/silicene oxide by separating them from the ML structures in the supernatant. With this process, converting CaSi<sub>2</sub> to Si MLs results in an ~96% yield, followed by a 3% yield for the transformation of Si MLs to silicene/silicene oxide. However, this latter yield can be increased if the precipitate is sonicated again followed by recollection of the supernatant. The materials obtained are mostly silicene layers though some oxidation has occurred during the process.

Figure 2 shows the scanning electron microscopy (SEM) images of CaSi<sub>2</sub> and of the products collected after each step of the silicene fabrication process. Figure 2a reveals the layered structure of the raw CaSi<sub>2</sub>, and Figure 2b shows the ML silicene/silicene oxide structure after Ca removal. In order to verify that calcium was completely removed from CaSi<sub>2</sub> in the silicene product, energy-dispersive X-ray mapping (EDX) for both CaSi<sub>2</sub> and ML silicene/silicene oxide was performed using a transmission electron microscope (TEM) (Supporting

Information, Figure S1). The EDX–TEM map of CaSi<sub>2</sub> shows very strong signals from calcium and silicon with a composition of 31 atom % for Ca and 63 atom % for Si, which is very close to the expected stoichiometry of CaSi<sub>2</sub>. The EDX–TEM mapping of the ML silicene shows no Ca signal, indicating that Ca has been completely removed. The high-resolution TEM (HRTEM) image for CaSi<sub>2</sub> (Supporting Information, Figure S2) shows a spacing of d=0.248 nm, which is consistent with the previously reported results for silicene sheets in CaSi<sub>2</sub>. Shows a spacing of d = 0.248 nm, which is consistent with the previously reported results for silicene sheets in CaSi<sub>2</sub>. To assess the quality of our starting material, X-ray diffraction (XRD) was performed on CaSi<sub>2</sub> (Supporting Information, Figure S3). The XRD pattern shows the characteristic sharp peaks for CaSi<sub>2</sub> in agreement with the JCPDS card no: 75-2192.

Figure 2d,g shows the TEM images of CaSi<sub>2</sub>, while Figure 2e,h shows the TEM images of ML silicene. From the crosssectional image for CaSi<sub>2</sub> (Figure 2g), one can see that the layers in CaSi2 are very closely packed, making it impossible to resolve the different layers of Si and Ca. Conversely, the crosssectional TEM image of ML silicene (Figure 2h) shows welldefined MLs of the silicene sheets. The SEM and TEM images of a few layers of silicene/silicene oxide after the tip sonication treatment are shown in Figure 2c,f,i, with the corresponding higher magnification TEM images shown in Figure S4 in the Supporting Information. HRTEM images (with the corresponding FFTs) were recorded for silicene (Supporting Information, Figure S5) where a lattice spacing of d = 0.21nm is shown. This spacing is consistent with the reported values for silicene<sup>24,36,37</sup> and is different from the value for bulk silicon (a diamond-type structure), which has a spacing of d = $0.31 \text{ nm.}^{3}$ 

Atomic force microscopy (AFM) characterization was conducted for the silicene/silicene oxide samples (Figure 3). As shown in Figure 3a, the ML silicene/silicene oxide is very thick (thickness > 100 nm) and has a staircase morphology indicative of a layered structure. Figure 3b,c shows the final product of the few-layer and single-layer silicene/silicene oxide with thicknesses of 2.5 and 0.8 nm, respectively, which is in agreement with the literature for few-layer and monolayer silicene. <sup>36,37,39</sup>

Raman spectroscopy was used to analyze CaSi<sub>2</sub> and the silicene products. The Raman spectrum of a Si wafer is used as a reference as shown in Figure S6 in the Supporting Information. Figure 4 shows the Raman peaks of raw CaSi<sub>2</sub> which are located at 336 cm<sup>-1</sup> (Ca–Si), 382 cm<sup>-1</sup> (Si–Si), and 408 cm<sup>-1</sup> (Ca–Si). The silicene sample has Raman modes at 380 cm<sup>-1</sup> (2D silicon planes), 495 cm<sup>-1</sup> (2D Si<sub>6</sub> rings) with a weak shoulder at 517 cm<sup>-1</sup> (associated with defects or D peak), 40 632 cm<sup>-1</sup> (SiH<sub>n</sub>), and 732 cm<sup>-1</sup> (SiH). We found that our silicene sample consists of a buckled Si monolayer that is mostly monohydride terminated, resembling silicon, which is consistent with the literature.

The degradation of silicene/silicene oxide over time was studied by Raman spectroscopy, as shown in Figure 5a. The Raman spectra were recorded for silicene samples of varying age, ranging from freshly prepared to 12 weeks old. The intensity ( $I_{\rm Si6}$ ) of the Raman peak at 495 cm<sup>-1</sup> (corresponding to the Si<sub>6</sub> rings) decreased over time, while the intensity ( $I_{\rm D}$ ) of the Raman peak at 517 cm<sup>-1</sup> (associated with defects) increased over time. After 6 weeks, most of the Si–H bonds in the Si<sub>6</sub> rings were no longer present. After 9 weeks, the ratio saturated and the Raman peak at 495 cm<sup>-1</sup> vanished along with a very strong defect peak at 517 cm<sup>-1</sup>. The silicene sample was

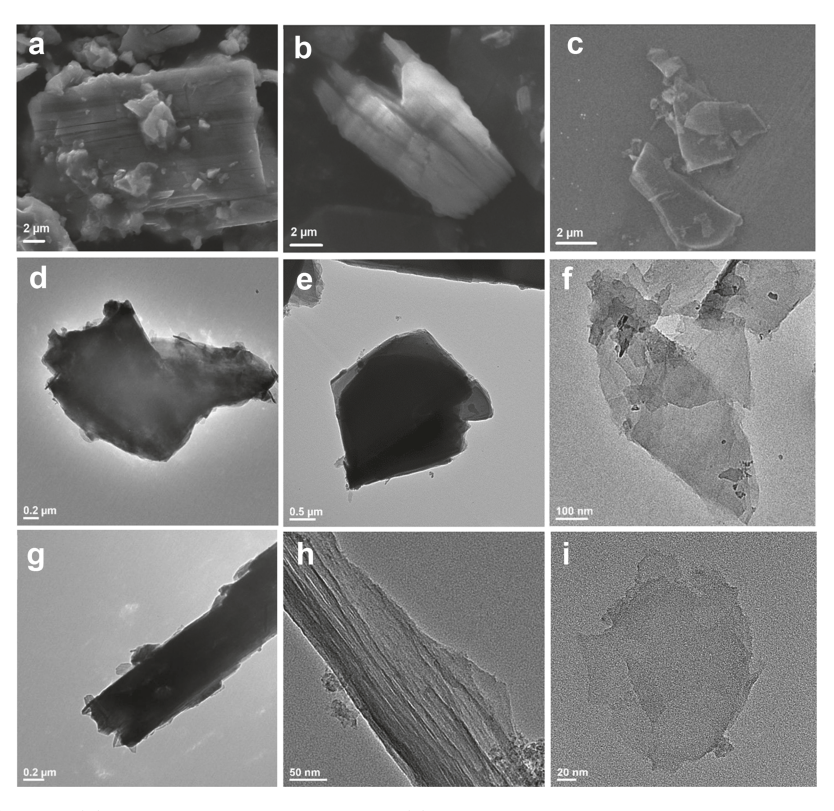


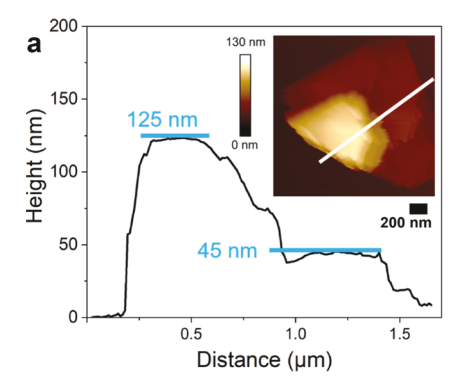
Figure 2. SEM images of (a) CaSi<sub>2</sub>, (b) ML silicene/silicene oxide, and (c) few-layer silicene/silicene oxide layers. TEM images of (d and g) CaSi<sub>2</sub>, (e and h) ML silicene/silicene oxide, and (f and i) few- or single-layer silicene/silicene oxide.

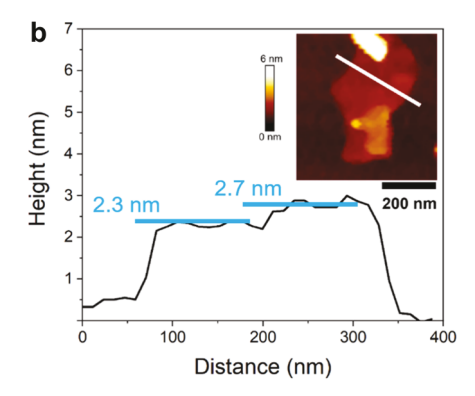
completely oxidized by 9-12 weeks, which indicates that silicene is sensitive to ambient conditions and tends to oxidize in air. Due to this sensitivity, we coated silicene with a thin layer of Al<sub>2</sub>O<sub>3</sub> in an attempt to insulate it from ambient air. In order to study the effectiveness of this protective Al<sub>2</sub>O<sub>3</sub> layer, an annealing experiment was performed with a bare and coated silicene sample. Annealing was performed in air at temperatures of 50 and 100 °C for 45 min. Figure S10 in the Supporting Information shows the Raman spectra of a silicene sample without the Al<sub>2</sub>O<sub>3</sub> (Figure S10a) coating and one with the coating (Figure S10b). Figure S10a shows that the bare sample has peaks consistent with natural silicene degradation in air, where the D peak is more dominant at 100 °C versus room temperature. This suggests that the annealed sample has a similar oxidation mechanism compared with the as-prepared sample oxidized under ambient conditions. Figure S10b, however, shows no major change in the Raman spectra of the coated sample even after it was annealed at 100 °C.

XPS (in high-resolution mode for Si 2p) was used to investigate the oxidation states of silicon in the silicene-containing samples during the degradation process. Figure 5b shows peaks at 99.6 and 100.4 eV, corresponding to Si 2p<sub>1/2</sub> and Si 2p<sub>3/2</sub>, respectively, and oxidized Si peaks at 101.9, 102.6, and 103.7 eV (for Si<sup>2+</sup>, Si<sup>3+</sup>, and Si<sup>4+</sup>, respectively). For the fresh and 3-week old samples, the Si<sup>0</sup> peak is clearly visible. The oxidized Si peak observed in the XPS spectra of the fresh sample is not surprising because the sample had been exposed to air before the XPS measurement. The peak from Si<sup>0</sup> gradually decreases over time and eventually vanishes after 12 weeks, while the Si<sup>4+</sup> and Si<sup>3+</sup> peaks are found to become more pronounced over time. In order to investigate the suboxide states, spectral deconvolution was performed using a Gaussian—Lorentzian function. By calculating the individual

suboxide  $(I_{\rm ox})$  contributions, where  $I_{\rm ox}$  is expressed by the ratio of the integrated area under its peak to the overall area, we calculate the overall oxide intensity  $I_{\rm tot} = I_{\rm SiO2} + I_{\rm Si2O3} + I_{\rm SiO}$  and obtained  $I_{\rm tot}$  values of 0.54, 0.71, 0.87, 0.94, and 1 for 0, 3, 6, 9, and 12 weeks, respectively. The XPS data indicate that the fresh sample is slightly oxidized due to air exposure, and the aged sample for 12 weeks is completely oxidized, which is consistent with the Raman measurements (Figure 5a). It should be pointed out that the oxidation of silicene did not change the morphology of the 2D layers as shown by the TEM images in Figure S7 in the Supporting Information for silicene aged for 12 weeks.

Computed Raman spectra were obtained to compare with the experiments to better understand the oxidation process. The calculations were carried out using a  $4 \times 5$  supercell of silicene. The degradation of silicene over time was modeled with several configurations, for example, adsorption of O atoms in random positions or O atoms for Si substitution. All these configurations were relaxed in a geometry optimization process, and then the Raman spectrum was obtained. Of all the configurations used, we only present geometries which closely match the experimental data (the details of which can be found in the Supporting Information). The other oxidation sites are considered less likely to be present under our experimental conditions. Figure 6 shows the calculated Raman spectra along with their corresponding atomic configurations. The atomic configurations show that the oxygen atoms are in a bridge-site environment, meaning that the oxygen atoms were placed over Si-Si bonds. More configurations of silicene with oxygen atoms are shown in Figure S8 in the Supporting Information along with explanations. For fresh silicene samples, the main peak appears at ~495 cm<sup>-1</sup> in the experiment and at 499.865 cm<sup>-1</sup> by theory. The percentage





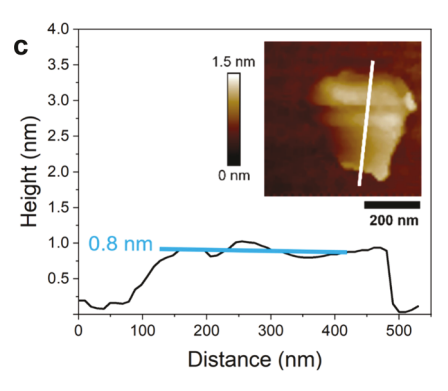


Figure 3. AFM images of silicene/silicene oxide: (a) ML, (b) few layer, and (c) single layer. The horizontal lines in a, b, and c indicate the thickness of multiple, few-layer, and single-layer silicene.

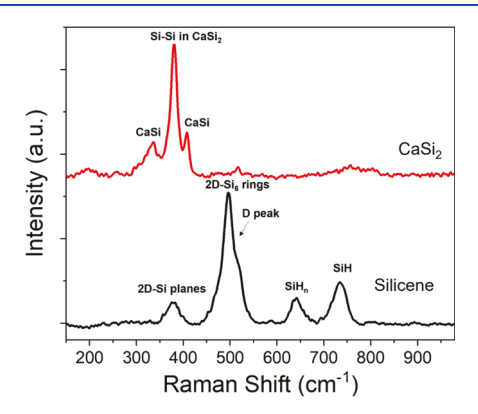


Figure 4. Raman spectra of CaSi<sub>2</sub> and silicene products.

error is 0.98%, reflecting the fact that the fresh silicene sample is relatively pure and closely matches the Raman spectrum of pristine silicene.

As soon as the oxygen atoms are introduced in the system, the D peak becomes more perceptible. This D peak occurs due to the in-plane vibrations, breathing modes, of the Si<sub>6</sub> rings and the oxygen atoms. The experimental spectrum at 3 weeks of aging closely matches with the computed spectrum of two oxygen atoms in opposite positions in the sample, giving an oxygen concentration of 4.76%. For the 6-week aged spectrum, a configuration of four oxygen atoms was obtained, two on each side, presenting a proportion of 9.09% oxygen. The 12weeks Raman spectrum could be simulated by a configuration of eight oxygen atoms placed on the silicon sheet. By increasing the oxygen atoms, the intensity of the shoulder peak is enhanced. The oxygen atoms are arranged in parallel positions in the bridge site with 16.67% of the oxygen on the sample. This shows that silicon-oxygen interactions are predominant for these longer-aged materials. Between pristine silicene and silicene aged for 12 weeks, the D peak translates along the x-axis by  $28 \text{ cm}^{-1}$ , as is expected. The orange lines in Figure 6 mark the D peak position.

The increase in the D peak intensity corresponds to an increase in the oxygen concentration, and so it can be concluded that the D peak is activated due to the presence of defects, as expected.<sup>44</sup> In samples with more defects induced by the oxygen atoms, the total momentum conservation is satisfied because one-phonon defect-assisted processes affect the D peak production and make this stand out. The other peaks are attenuated such that they are not noticeable. Another exciting observation in the fresh and 3-week-old silicene samples is that the D peak has two components, separated by 4.37 cm<sup>-1</sup>, which is much smaller than expected if a comparison is made with graphene. These two components are almost indistinguishable, together looking like a single broad peak (Figure 6). These two components are produced because the electron and hole momenta have different magnitudes because they occur from intervalley scattering. This intervalley scattering appears because the electron and hole have different momenta and one or both may experience a momentum change during Raman scattering. When oxidation occurs, the intervalley scattering with different momenta is eliminated, and the D peak is visibly narrower without the double component.44

As previously mentioned, oxygen atoms were introduced in various configurations (Supporting Information, Figure S8 and Table S1) by either substituting Si atoms for O atoms, cluster adsorption, or by placing oxygen atoms in random positions. The most stable configurations are the systems that have the oxygen atoms in random positions. These also happen to be the configurations that best match the experimental results. This means that the Si-O bonds are more significant than the O-O bonds. The adsorption energies of silicene- $O_2$ , silicene-O<sub>4</sub>, and silicene-O<sub>8</sub> are 1.24, 1.16, and 1.080 eV, respectively, showing a decrease in the adsorption energy as the concentration of oxygen increases. From the magnitudes of these energies, it can be deduced that the bonding is due to dipole attraction between molecules without becoming a van der Waals interaction or a covalent bond. On the other hand, Si-O bonds are still more significant than Si-Si bonds, demonstrated by the fact that the introduction of oxygen atoms causes the planar structure of silicene to be lost. The surface of the silicene layer bends due to the adsorption of oxygen atoms so that as the sample ages, a significant beak in symmetry occurs in the silicene lattice.

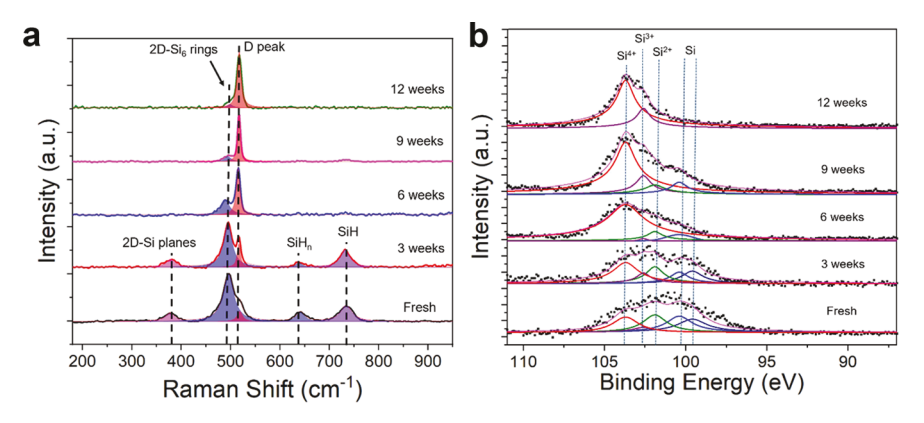
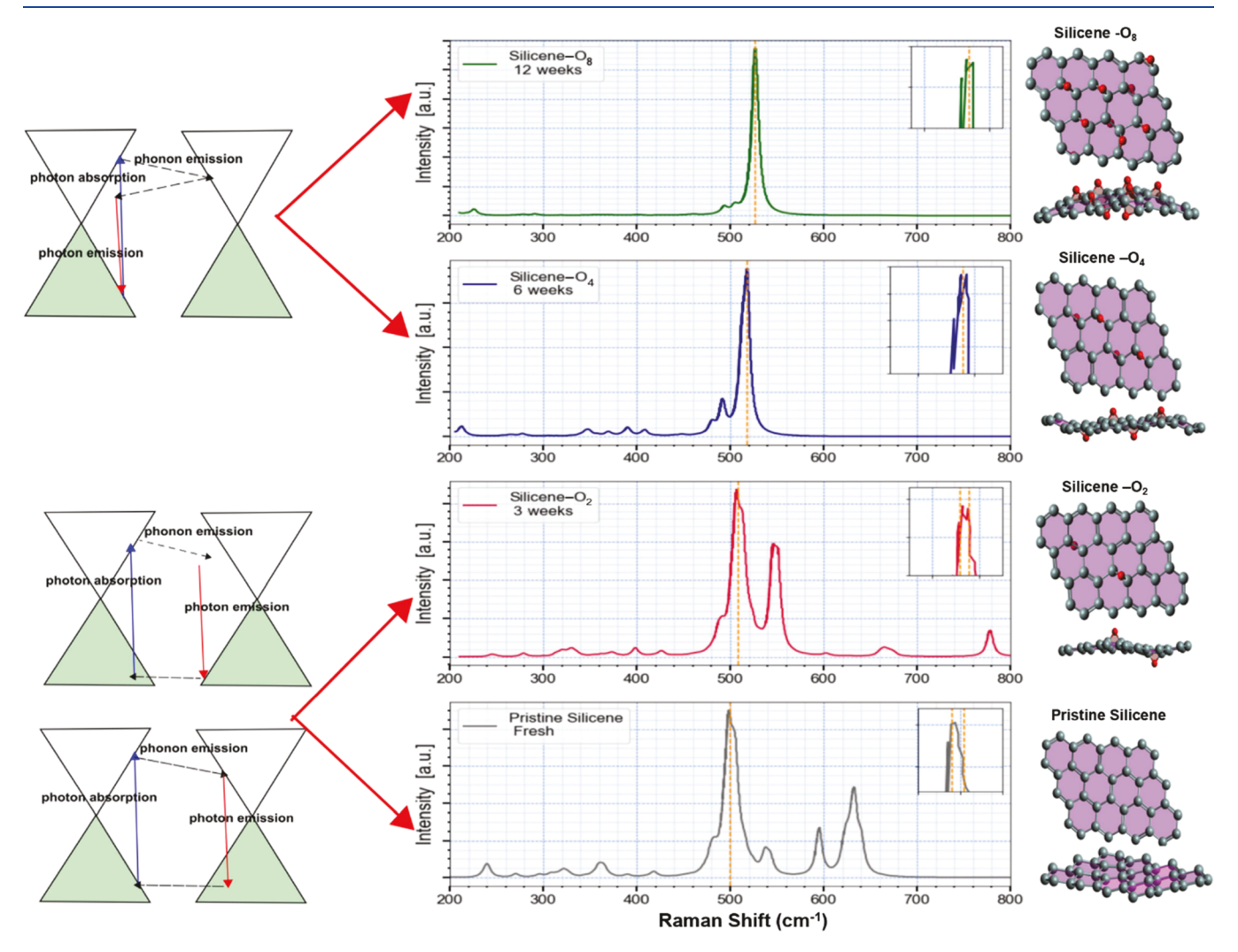


Figure 5. (a) Raman spectra of silicene degraded for different times and (b) X-ray photoelectron spectroscopy (XPS) spectra of Si 2p from silicene degraded for different times.



**Figure 6.** Computed Raman spectra and the corresponding atomic configurations for fresh and aged silicene. The gray and red dots represent silicon and oxygen atoms, respectively. The most probable intervalley scattering, consequence of the presence of defects, and the occurrence of the double component on the D peak are also shown. The cones represent electron dispersion and the green triangles are the occupied states.

Covalent functionalization, noncovalent functionalization, and elemental doping are three methods used to functionalize two-dimensional materials such as graphene and silicene. These functionalization methods have been shown to be effective at controlling of the quantity and quality of oxidation in graphene, and as such, we explored them for silicene surfaces. <sup>45</sup> Also, it is known that the oxidation of silicene

samples starts after 3 min of exposure to air. 46 By the procedure in which we obtained our samples, from the adsorption energies, and chemical bonding, it can be seen that this functionalization is primarily due to doping. To ensure the above and to better understand how this oxidation occurs, a DOS and PDOS analysis was carried out. It is known that the DOS and PDOS of two-dimensional surfaces give information

about how the charge is transported between the dopant or adsorbate with a two-dimensional surface and how the binding occurs. PDOS indicates the orbital contribution of each atom to the total DOS. The DOS of the pristine silicene, silicene— $O_2$ , silicene— $O_4$ , and silicene— $O_8$  is shown in Figure 7. The

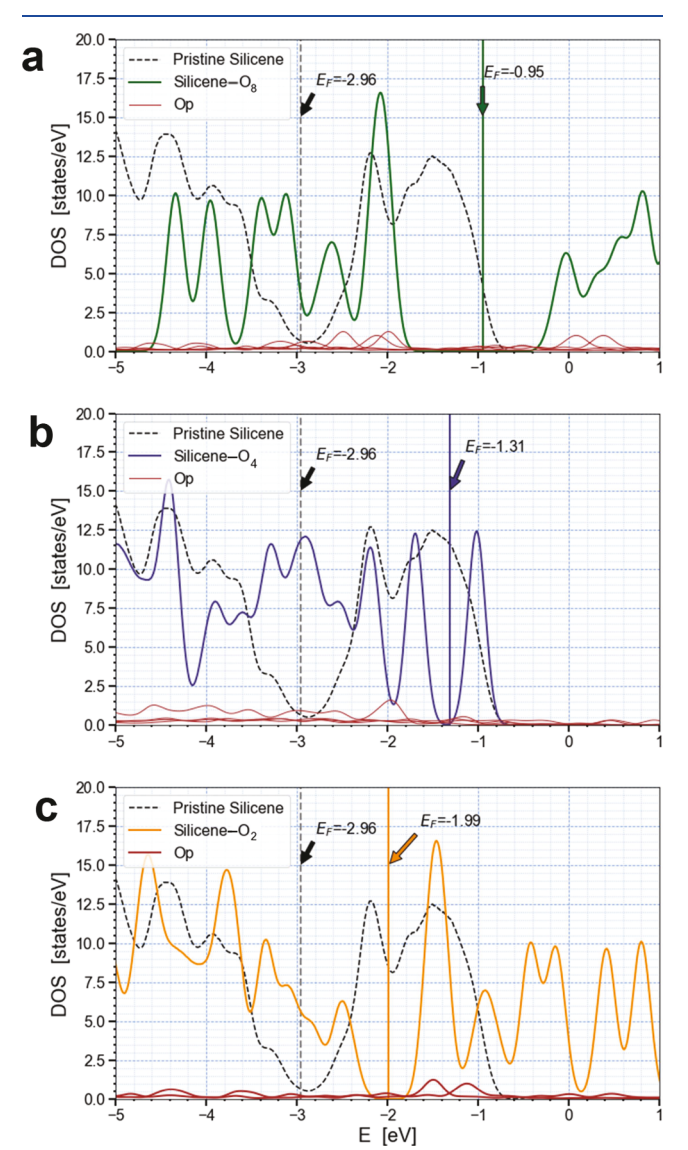


Figure 7. Total density of states (DOS) of silicene and partial density of states (PDOS) of the oxygen atoms absorbed by the silicene sheet. (a) The DOS of silicene with two oxygen atoms adsorbed, (b) with four oxygen atoms adsorbed, and (c) with eight oxygen atoms absorbed. In all cases, the DOS of pristine silicene is shown in black to better illustrate the effect of degradation.

DOS of pristine silicene (black line) has been placed against the DOS of silicene with oxygen atoms to observe the effect of the degradation process at an electronic level. The 2p electrons of oxygen atoms are shown in brown to analyze their effects in the total DOS spectrum. The electrons in the 2s levels are not shown because they do not affect the electronic behavior. Also, the total DOS is represented and not separated by spins up and down since these spectra are identical. No magnetization is shown in the system. The DOS of the pristine silicene shows an analogous behavior to pristine graphene, with a Dirac cone associated with the Fermi level. After oxygen adsorption, it is

noticed that the 2p electrons contribute to the occupied states in the neighborhood of the Fermi energy  $(E_{\rm F})$ , improving the semiconductor behavior. Likewise, as the oxygen atoms are introduced to silicene, the electronic band gap is modified. The band gap for silicene, silicene– $O_2$ , silicene– $O_4$ , and silicene– $O_8$  are 0.0011, 0.1971, 0.102, and 1.1056 eV, respectively. As the samples become oxidized, the band gap shows a tendency to increase slightly. Therefore, silicene oxide remains a narrow band gap material. UV—vis spectroscopy measurements show that silicene exhibits a quick increase of absorption in the short wavelength (Supporting Information, Figure S9). This absorption is directly associated with the responsivity quantum efficiency of photodetectors as discussed in the next few paragraphs.

DOS analysis is a valuable tool used to understand the charge transfer mechanism in the bonding which occurs during the oxidation process. The difference in Fermi energies between pristine silicene and silicene-O<sub>n</sub> gives quantitative information on how charge transfer occurs. The  $E_F$  values are -2.96, -1.99, -1.31, and -0.95 eV for pristine silicene, silicene-O<sub>2</sub>, silicene-O<sub>4</sub>, and silicene-O<sub>8</sub>, respectively, which result in Fermi energies differences ( $\Delta E_{\rm F}$ ) of -0.97, -1.65, and -2.01 eV for silicene-O2, silicene-O4, and silicene-O8. This shows that the charge goes from the oxygen atoms to the silicene surface, making the silicene surface negatively charged and more attractive to other possible dopants as would be the case with more oxygen atoms. Figure 7 clearly shows the oxygen atoms affecting the Fermi energy, causing more states to be available to form a bond, which is weak. Therefore, since the oxygen states actively affect the Fermi energy of the systems, we conclude that the oxidation mechanism is elemental doping, which agrees with the minimum energy structures, the adsorption energies, and the experimental results.

A broadband photodetector device was fabricated with an interdigitated gold electrode on a silicon wafer with a thin SiO<sub>2</sub> layer. The separation between the gold electrodes (channel length) is 3  $\mu$ m. Silicene was deposited on this electrode via the drop-casting method. In order to protect the sample from degradation, 15 nm of aluminum oxide (Al<sub>2</sub>O<sub>3</sub>) was deposited on top of the silicene layer at 150 °C using an ALD system. More details can be found in the Experimental Section. This coating provides good protection for silicene against degradation. Figure 8a shows a schematic diagram of the photodetector device. The inset of Figure 8a is an optical image of silicene deposited between the interdigitated gold electrodes. The thickness of silicene was determined by AFM and was found to be 2.5 nm. In general, the excitons in silicene can be generated under light illumination. The electron-hole pairs may be dissociated under an applied bias due to the defect-related trap states in silicene. The holes and electrons are then expected to move to the cathode and anode, respectively, generating a photocurrent.

Figure 8b shows the semilogarithmic current density versus voltage (J-V) curve of the device in the dark and under 404 nm excitation with voltage sweeping from -2 to 2 V. The dark J-V curve shows the presence of a dark leakage current of 30 mA/cm<sup>2</sup> at a voltage of 2 V. Under an illumination power of 20 mW, the photogenerated current reaches 100 mA/cm<sup>2</sup>, which is about 30 times higher than the dark current. The device was tested with 404 nm illumination at different powers ranging from 1 to 50 mW. Figure 8c shows the current responses to the ON/OFF state of light illumination at different laser powers.

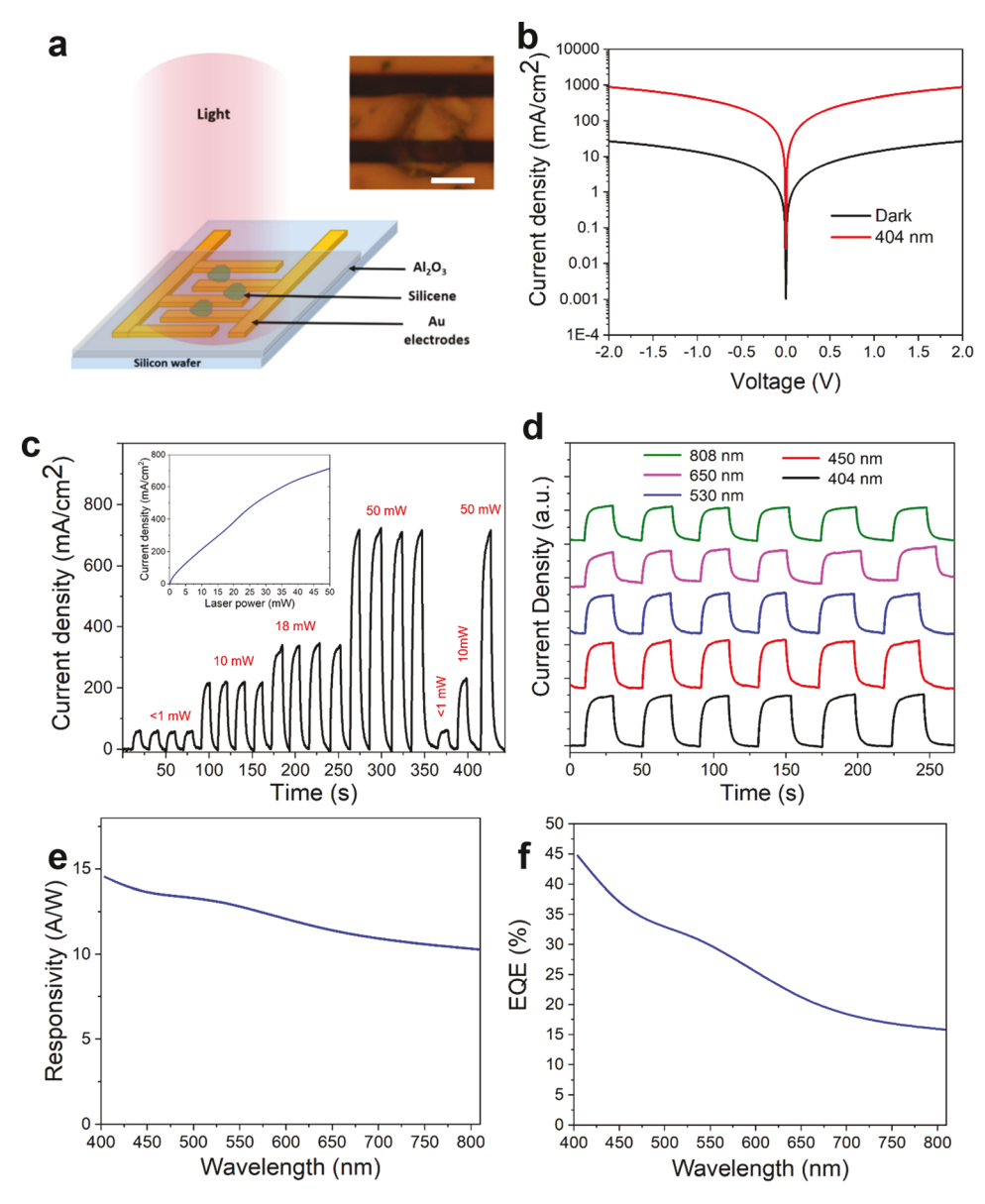


**Figure 8.** (a) Schematic diagram of the photodetector device structure consisting of a silicene layer between interdigitated electrodes with light from the top. The inset shows a photograph of the device taken under an optical microscope (scale bar:  $5 \mu m$ ); (b) semilogarithmic J-V plot of the device in the dark and under 404 nm light illumination; (c) ON–OFF responses of the photodetector to different laser powers of 404 nm. The inset is a curve of current density versus laser power; (d) ON–OFF responses to different laser wavelengths; (e) responsivity versus wavelength; and (f) external quantum efficiency (EQE) versus wavelength.

The device shows stable oscillations with consistent currents at each laser power. When the laser power was reset back to 1, 10, and 50 mW, the photocurrents repeated their patterns of oscillations. The inset of Figure 8c shows photocurrent as a function of illumination power. One can see that a linear relationship is obtained between current and light power when the power is below 30 mW. Above this power, a nonlinear behavior is observed. The increase in photocurrent tends to become slower at high power due to a saturation process.

Figure 8d shows the photocurrent response to light illumination of different wavelengths. The device shows similar current oscillations with different wavelengths; however, the short wavelength illumination causes relatively larger photocurrents. This is likely related to the wavelength-dependent absorption of silicene. As shown in Figure S9 of the Supporting

Information, silicene has broad absorption which provides the observed photoresponse in a wide range of the spectrum.

There are three main parameters that are used to evaluate the performance of photodetectors: responsivity (R), detectivity (D), and EQE. The details on the definition of these quantities are provided in Supplemental Note 1. Figure 8e shows the responsivity of the silicene photodetector as a function of wavelength. It shows that the responsivity increases continuously as the light wavelength decreases from 800 nm (10 A/W) down to 404 nm (14.5 A/W). The responsivity is very high compared to other silicon-based nanomaterials as illustrated in Table 1. Figure 8f shows the EQE of the silicene photodetector as a function of wavelength. Again, the EQE value is found to increase as the wavelength decreases from 800 nm (15%) down to 404 nm (45%). This significant

Table 1. Comparison Table of Photodetectors with Other Materials

material	detection range	responsivity (A/W)	detectivity (Jones)	EQE (%)	response time	ref
graphene	457-785 nm	$4 \times 10^{-3}$				53
N-graphene QDs	300-1000 nm	325			50 s, 10 s	54
GaTe	254-710 nm	274.3				55
GaSe	254-700 nm	2.8		1367	20 ms	56
GaS	254-610 nm	$5.06 \times 10^{-4}$				57
Si <sub>3</sub> N <sub>4</sub> film	UV	0.325		3.07	19.3 s, 1.8 s	58
$MoS_2$	380-700 nm	0.57			$70-110 \ \mu s$	59
silicon nanoparticles	200-600 nm	0.75	$\sim 10^{12}$			60
silicon nanowire	632 nm	0.067	$5.2 \times 10^9$	13.24		61
silicon nanowires	near IR	0.386				62
pSi-graphene	400-500 nm	0.2			3 μs	63
Si NS in a polymer matrix	UV					49
[Si <sub>6</sub> H <sub>4</sub> Ph <sub>2</sub> ] sheets	vis					39
silicene/silicene oxide few layers	400-808 nm	14.53	$3.01 \times 10^{10}$	44.61	1.6 s, 1.4 s	this wor

increase is likely associated with the intrinsic absorption of silicene as shown in Figure S9 in the Supporting Information.

There is very limited literature on silicene photodetectors. Lugli and his group reported photodetectors using 2D silicon sheet composites, which were made by mixing 2D silicon sheets with tert-butyl methacrylate on gold electrodes. They observed a photoresponse but did not provide the values of R, D, or EQE.<sup>49</sup> Nakano and co-workers reported 2D silicon sheets of organosilicon functionalized with phenyl groups and showed a photoresponse in a photoelectrochemical cell. Again they did not report the R, D, and EQE values.<sup>39</sup> Table 1 lists the performance of several silicon nanomaterial-based photodetectors, including silicon nanoparticles, nanowires, Sigraphene mixture, and silicon nanosheets in a polymer matrix. Most of the other silicon materials show low responsivity. The silicon nanoparticles have a broad band response and very high detectivity, but the EQE value is not available. Kharadi et al. laid the foundations of a silicene photodetector based on a computational approach and designed a photodetector with silicene nanoribbons functionalized with Li and Cl. Their device structure has infinite silicene electrodes with the silicene nanoribbons functionalized with Li and Cl. They calculated the detectivity value in the order of 1012 under 0.09 mW/nm2 illumination at 1100 nm. This showed that silicene is an excellent candidate for photodetectors due to the excellent performance compared to photodetectors made using other 2D materials.<sup>50</sup> However, our study provides the first experimental demonstration that silicene photodetectors have an excellent performance. The degradation of silicene is expected to change the device performance. This was demonstrated by annealing the devices in air to induce oxidation of silicene. Figure S11 in the Supporting Information shows a comparison of the photoresponses from the asprepared and annealed silicene photodetector at 50 and 100 °C.

As is well known, the photoresponse time is an important parameter for a photodetector. The dynamic rise and decay is expected to follow the equations  $I = I_0(1 - \mathrm{e}^{t_r})$  and  $I = I_0\mathrm{e}^{t_r}$ , where  $t_r$  and  $t_f$  are time constants for the rise and decay processes, respectively. Figure S12 in the Supporting Information shows the experimental data from the photodetector device and the corresponding fittings using these exponential functions. The time constants,  $t_r$  and  $t_f$  were found to be 1.6 and 1.4 s, respectively.

As shown in Table 1, the silicene-based devices based on this study show a wide detection range, very high responsivity, high detectivity, and high quantum efficiency and moderate response time. The responsivity of silicene is about 20 times higher than silicon nanoparticles and more than 200 times higher than silicon nanowires in the visible range. Its EQE is four times higher than the available value for silicon nanowires. One can see that the silicene photodetectors have an outstanding performance in all of the above categories, which require further improvement and optimization for practical applications.

#### 3. CONCLUSIONS

In conclusion, we have fabricated relatively large quantities of single/few layers of silicene/silicene oxide with the deintercalation of calcium from CaSi2. These silicene/silicene oxide layers have been extensively characterized using a combination of SEM, TEM, EDX, XPS, and Raman microscopy/spectroscopy. These studies suggest that the freshly made silicene is pristine but highly oxidized after 12 weeks of storage as reflected by the Raman peak at 517 cm<sup>-1</sup> associated with the defects in the silicene layers. However, TEM images show that the oxidized silicene still retains its 2D morphology. The oxidative degradation of silicene was also studied with a density functional theory (DFT) calculation, which agrees with the experimental observations. We demonstrate the outstanding performance of silicene as a broadband photodetector with superior responsivity, detectivity, and EQE compared with other silicon nanomaterial-based devices.

#### 4. EXPERIMENTAL SECTION/METHODS

**4.1. Materials and Equipment.**  $CaSi_2$  and concentrated HCl were purchased from Sigma-Aldrich, and trimethylaluminum (TMA) was obtained from Strem Chemicals Inc.

Material characterization was performed with an FEI Quanta 200 SEM with an energy-dispersive X-ray spectroscope (EDX), a JEOL JEM-2100 TEM, a PHI 5000 Versa Probe scanning X-ray photoelectron spectroscope (XPS), an Agilent Technologies Cary 60 UV—vis spectrometer, a RENISHAW inVia Raman microscope with an excitation of 532 nm, and a Veeco Multimode Nanoscope III AFM. The  $Al_2O_3$  protection coating was deposited by a Veeco Savannah ALD system. The optoelectrical properties were measured with a Keithley 4200 semiconductor analyzer.

**4.2. Experimental Procedure.** A total of 0.05 g of  $CaSi_2$  was kept for 3 days in HCl at -10 °C under continuous stirring. Silicene/silicene oxide MLs were separated by centrifugation at 6000 rpm for

10 min. The supernatant was removed, and the precipitate was dispersed in ethanol for centrifugation. This process was repeated five times, after which the sample was dried in vacuum for 3 days. At this stage, silicene MLs were obtained. To achieve few- and single-layer silicene, the MLs were dispersed in methanol and placed in a tip sonicator at 1 W for 1 h in an ice bath. Finally, the single-layer, few-layer, and ML products were separated by centrifugation at 6000 rpm for 2 min, after which the thin silicene flakes of few and single layers were obtained in the supernatant.

Device fabrication was achieved by using an interdigitated chip configuration with gold electrodes of 100 nm thickness on a P-type monocrystalline silicon wafer with 300 nm  ${\rm SiO_2}$ . The separation between the electrodes was 3  $\mu$ m. Silicene/silicene oxide was deposited onto this electrode via a drop-casting method by transferring 2  $\mu$ L of single–few layers silicene/silicene oxide onto the chip with gold electrodes and drying it in vacuum. The few–single layers have a thickness in the range of 0.8 to about 2.5 nm. Finally, a 15 nm  ${\rm Al_2O_3}$  coating was deposited at 150 °C by ALD using TMA as an aluminum source and  ${\rm H_2O}$  as an oxygen source with  ${\rm N_2}$  as the carrier gas. In order to obtain a 15 nm coating, 150 cycles were used with each cycle consisting of a pulse duration of 0.015 s for TMA, 0.015 s for  ${\rm H_2O}$ , and a wait time of 3 s between pulses.

For the Raman measurements, silicene/silicene oxide was placed on glass substrates using a drop-casting method. The laser spot size was  $\sim\!\!30~\mu\text{m}^2$  with a laser power of 1 mW. During the XPS measurement, Al monochromatic X-ray radiation (1486.7 eV) was focused to a spot size of about 200  $\mu\text{m}^2$  and the pressure of the target chamber was maintained at  $9\times10^{-9}$  mbar. Ar sputtering was not used before the measurement. TEM was conducted with a JEOL JEM-2100 with an operation voltage of 200 kV. The TEM sample was prepared by drop-casting on the carbon-coated 200 mesh copper grid and dried in vacuum. XRD for CaSi<sub>2</sub> was performed using Cu K $\alpha$  1.541 Å radiation with a Rigaku Ultima III high-resolution X-ray diffractometer. The AFM images were measured using the tapping mode with silicon AFM tips purchased from Ted Pella Inc.

- **4.3. Device Characterization.** The photodetector device was placed in a device-under-test box with spring-loaded contacts. A Keithley 4200 semiconductor analyzer was used as a source measure unit. Different laser powers at wavelengths of 404, 450, 530, 650, and 808 nm were modulated with a step variable neutral density filter and measured with a power meter. Finally, the device performance was evaluated and calculated based on Supplemental Note 1.
- 4.4. Computational Methods. The calculations were performed with the Quantum Espresso computational package<sup>64</sup> in the DFT theory framework with a plane-wave basis set and pseudopotentials. The functional was generalized gradient approximation, in particular, the Perdew-Burke-Ernzerhof exchange-correlation functional.<sup>65</sup> An empirical dispersion correction was used with Grimme's method D3-BJ. The Kohn-Sham orbitals were expanded using a kinetic energy cutoff of 50 Ry (around 681 eV), and the convergence criterion was 10<sup>-8</sup> Ry. Brillouin zone integrations were performed by applying the Methfessel-Paxton smearing special-point technique with a parameter of 0.05 Ry.<sup>67</sup> The k-point selection was made based on a Monkhorst-Pack G-centered  $8 \times 8 \times 1$  k-point mesh. The pseudopotential was the projector augmented wave method.<sup>68</sup> The phonon wavenumber calculations for the Raman spectra were performed with the optimized structure with the LDA functional, norm-conserving pseudopotentials.

## ASSOCIATED CONTENT

#### Supporting Information

The Supporting Information is available free of charge at https://pubs.acs.org/doi/10.1021/acsanm.2c00337.

SEM and TEM, XRD and EDX for the starting material, HRTEM for silicene/silicene oxide, Raman and TEM for silicene degradation, and device stability with the photoresponse time (PDF)

#### AUTHOR INFORMATION

#### **Corresponding Author**

Jingbiao Cui — Department of Physics, University of North Texas, Denton, Texas 76203, United States; orcid.org/0000-0003-3408-1016; Email: jingbiao.cui@unt.edu

#### **Authors**

Roberto Gonzalez-Rodriguez — Department of Physics, University of North Texas, Denton, Texas 76203, United States; © orcid.org/0000-0001-6849-1799

Roxana M. del Castillo – Departamento de Física, Facultad de Ciencias, Universidad Nacional Autónoma de México, CDMX 04510, Mexico; orcid.org/0000-0002-1670-8631

Evan Hathaway – Department of Physics, University of North Texas, Denton, Texas 76203, United States

Yuankun Lin — Department of Physics, University of North Texas, Denton, Texas 76203, United States

Jeffery L. Coffer – Department of Chemistry and Biochemistry, Texas Christian University, Fort Worth, Texas 76129, United States; ⊚ orcid.org/0000-0003-0267-9646

Complete contact information is available at: https://pubs.acs.org/10.1021/acsanm.2c00337

#### **Author Contributions**

J.C. directed and supervised the project. R.G.-R. initialized this project and fabricated and characterized the material/device. R.d.C. worked on the theoretical calculations. J.L.C, E.H., and Y.L. were involved in the data analysis and discussion. All authors contributed to discussions and finalization of the manuscript.

#### Notes

The authors declare no competing financial interest.

## ACKNOWLEDGMENTS

This work was supported by the U.S. National Science Foundation (#2128367) and Dirección General de Asuntos del Personal Académico (# IN120120). It was carried out using a Miztli HP Cluster 3000 supercomputer, provided by Dirección General de Cómputo y Tecnologías de Información y Comunicación (DGTIC) and Universidad Nacional Autónoma de México (UNAM) with the project LANCAD-UNAM-DGTIC-385.

#### REFERENCES

- (1) Novoselov, K. S.; Geim, A. K.; Morozov, S. V.; Jiang, D.; Zhang, Y.; Dubonos, S. V.; Grigorieva, I. V.; Firsov, A. A. Science 2004, 306, 666.
- (2) Rowley-Neale, S. J.; Randviir, E. P.; Abo Dena, A. S.; Banks, C. E. Appl. Mater. Today 2018, 10, 218–226.
- (3) Lin, L.-C.; Grossman, J. C. Nat. Commun. 2015, 6, 8335.
- (4) Liu, X.; Xu, T.; Wu, X.; Zhang, Z.; Yu, J.; Qiu, H.; Hong, J.-H.; Jin, C.-H.; Li, J.-X.; Wang, X.-R.; Sun, L.-T.; Guo, W. Nat. Commun. **2013**, *4*, 1776.
- (5) Nakamura, D.; Nakano, H. Chem. Mater. 2018, 30, 5333-5338.
- (6) Takahashi, M. Sci. Rep. 2017, 7, 10855.
- (7) Chang, D. W.; Choi, H.-J.; Filer, A.; Baek, J.-B. J. Mater. Chem. A **2014**, 2, 12136–12149.
- (8) Liu, J.; Yang, Y.; Lyu, P.; Nachtigall, P.; Xu, Y. Adv. Mater. 2018, 30, No. 1800838.
- (9) Zhuang, J.; Xu, X.; Peleckis, G.; Hao, W.; Dou, S. X.; Du, Y. *Adv. Mater.* **2017**, 29, No. 1606716.
- (10) Koh, K. H.; Noh, S. H.; Kim, T.-H.; Lee, W. J.; Yi, S.-C.; Han, T. H. RSC Adv. **2017**, 7, 26113–26119.

- (11) Gupta, S. K.; Singh, D.; Rajput, K.; Sonvane, Y. RSC Adv. 2016, 6, 102264–102271.
- (12) Liu, N.; Qiao, H.; Xu, K.; Xi, Y.; Ren, L.; Cheng, N.; Cui, D.; Qi, X.; Xu, X.; Hao, W.; Dou, S. X.; Du, Y. Small 2020, 16, No. 2000283.
- (13) Cinquanta, E.; Scalise, E.; Chiappe, D.; Grazianetti, C.; van den Broek, B.; Houssa, M.; Fanciulli, M.; Molle, A. *J. Phys. Chem. C* **2013**, *117*, 16719–16724.
- (14) Feng, B.; Ding, Z.; Meng, S.; Yao, Y.; He, X.; Cheng, P.; Chen, L.; Wu, K. Nano Lett. **2012**, *12*, 3507–3511.
- (15) Hogan, C.; Pulci, O.; Gori, P.; Bechstedt, F.; Martin, D. S.; Barritt, E. E.; Curcella, A.; Prevot, G.; Borensztein, Y. *Phys. Rev. B* **2018**, 97, No. 195407.
- (16) Enriquez, H.; Vizzini, S.; Kara, A.; Lalmi, B.; Oughaddou, H. J. Phys.: Condens. Matter 2012, 24, No. 314211.
- (17) Meng, L.; Wang, Y.; Zhang, L.; Du, S.; Wu, R.; Li, L.; Zhang, Y.; Li, G.; Zhou, H.; Hofer, W. A.; Gao, H.-J. *Nano Lett.* **2013**, *13*, 685–690.
- (18) Enriquez, H.; Mayne, A.; Kara, A.; Vizzini, S.; Roth, S.; Lalmi, B.; Seitsonen, A. P.; Aufray, B.; Greber, T.; Belkhou, R.; Dujardin, G.; Oughaddou, H. *Appl. Phys. Lett.* **2012**, *101*, No. 021605.
- (19) Quhe, R.; Yuan, Y.; Zheng, J.; Wang, Y.; Ni, Z.; Shi, J.; Yu, D.; Yang, J.; Lu, J. Sci. Rep. **2014**, *4*, 5476.
- (20) Du, Y.; Zhuang, J.; Wang, J.; Li, Z.; Liu, H.; Zhao, J.; Xu, X.; Feng, H.; Chen, L.; Wu, K.; Wang, X.; Dou, S. X. Sci. Adv. 2016, 2, No. e1600067.
- (21) Rachid Tchalala, M.; Enriquez, H.; Mayne, A. J.; Kara, A.; Roth, S.; Silly, M. G.; Bendounan, A.; Sirotti, F.; Greber, T.; Aufray, B.; Dujardin, G.; Ait Ali, M.; Oughaddou, H. *Appl. Phys. Lett.* **2013**, *102*, No. 083107.
- (22) Fleurence, A.; Friedlein, R.; Ozaki, T.; Kawai, H.; Wang, Y.; Yamada-Takamura, Y. Phys. Rev. Lett. 2012, 108, No. 245501.
- (23) Tsoutsou, D.; Xenogiannopoulou, E.; Golias, E.; Tsipas, P.; Dimoulas, A. Appl. Phys. Lett. 2013, 103, 231604.
- (24) Ali, M. A.; Tchalala, M. R. J. Phys.: Conf. Ser. 2014, 491, No. 012009.
- (25) Fuchs, H. D.; Stutzmann, M.; Brandt, M. S.; Rosenbauer, M.; Weber, J.; Breitschwerdt, A.; Deák, P.; Cardona, M. *Phys. Rev. B* 1993, 48, 8172–8189.
- (26) Okamoto, H.; Kumai, Y.; Sugiyama, Y.; Mitsuoka, T.; Nakanishi, K.; Ohta, T.; Nozaki, H.; Yamaguchi, S.; Shirai, S.; Nakano, H. *J. Am. Chem. Soc.* **2010**, *132*, 2710–2718.
- (27) Molle, A.; Faraone, G.; Lamperti, A.; Chiappe, D.; Cinquanta, E.; Martella, C.; Bonera, E.; Scalise, E.; Grazianetti, C. Faraday Discuss. 2021, 227, 171–183.
- (28) Wang, F.; Luo, P.; Zhang, Y.; Huang, Y.; Zhang, Q.; Li, Y.; Zhai, T. Sci. China Mater. 2020, 63, 1537–1547.
- (29) Liu, R.; Wang, F.; Liu, L.; He, X.; Chen, J.; Li, Y.; Zhai, T. Small Struct. **2021**, 2, No. 2000136.
- (30) Li, H.; Wang, Y.; Dai, X.; Gao, Y.; Lu, G.; Fang, Z.; He, H.; Huang, J.; Ye, Z. J. Mater. Chem. C 2021, 9, 10065–10072.
- (31) Sun, W.; Yan, X.; Qian, C.; Duchesne, P. N.; Hari Kumar, S. G.; Ozin, G. A. Faraday Discuss. **2020**, 222, 424–432.
- (32) Zhuang, J.; Xu, X.; Feng, H.; Li, Z.; Wang, X.; Du, Y. Sci. Bull. 2015, 60, 1551–1562.
- (33) Vogt, P.; De Padova, P.; Quaresima, C.; Avila, J.; Frantzeskakis, E.; Asensio, M. C.; Resta, A.; Ealet, B.; Le Lay, G. *Phys. Rev. Lett.* **2012**, *108*, No. 155501.
- (34) Castillo, S. M.; Tang, Z.; Litvinchuk, A. P.; Guloy, A. M. *Inorg. Chem.* **2016**, *55*, 10203–10207.
- (35) Krishnamoorthy, K.; Pazhamalai, P.; Kim, S.-J. *Energy Environ. Sci.* **2018**, *11*, 1595–1602.
- (36) Xu, X.; Zhou, L.; Ding, D.; Wang, Y.; Huang, J.; He, H.; Ye, Z. ACS Appl. Nano Mater. **2020**, *3*, 538–546.
- (37) Kara, A.; Enriquez, H.; Seitsonen, A. P.; Voon, L. C. L. Y.; Vizzini, S.; Aufray, B.; Oughaddou, H. Surf. Sci. Rep. 2012, 67, 1–18. (38) Lang, J.; Ding, B.; Zhang, S.; Su, H.; Ge, B.; Qi, L.; Gao, H.; Li, X.; Li, Q.; Wu, H. Adv. Mater. 2017, 29, No. 1701777.

- (39) Sugiyama, Y.; Okamoto, H.; Mitsuoka, T.; Morikawa, T.; Nakanishi, K.; Ohta, T.; Nakano, H. J. Am. Chem. Soc. **2010**, 132, 5946–5947.
- (40) Scalise, E.; Houssa, M.; Pourtois, G.; van den Broek, B.; Afanas'ev, V.; Stesmans, A. Nano Res. 2013, 6, 19-28.
- (41) Ryan, B. J.; Hanrahan, M. P.; Wang, Y.; Ramesh, U.; Nyamekye, C. K. A.; Nelson, R. D.; Liu, Z.; Huang, C.; Whitehead, B.; Wang, J.; Roling, L. T.; Smith, E. A.; Rossini, A. J.; Panthani, M. G. *Chem. Mater.* **2020**, 32, 795–804.
- (42) Bashouti, M. Y.; Sardashti, K.; Ristein, J.; Christiansen, S. H. Phys. Chem. Chem. Phys. 2012, 14, 11877–11881.
- (43) Sublemontier, O.; Nicolas, C.; Aureau, D.; Patanen, M.; Kintz, H.; Liu, X.; Gaveau, M.-A.; Le Garrec, J.-L.; Robert, E.; Barreda, F.-A.; Etcheberry, A.; Reynaud, C.; Mitchell, J. B.; Miron, C. *J. Phys. Chem. Lett.* **2014**, *5*, 3399–3403.
- (44) Ferrari, A. C.; Basko, D. M. Nat. Nanotechnol. 2013, 8, 235-246.
- (45) Yu, W.; Sisi, L.; Haiyan, Y.; Jie, L. RSC Adv. 2020, 10, 15328–15345.
- (46) Molle, A.; Grazianetti, C.; Chiappe, D.; Cinquanta, E.; Cianci, E.; Tallarida, G.; Fanciulli, M. *Adv. Funct. Mater.* **2013**, 23, 4340–4344.
- (47) Del Castillo, R. M.; Sansores, L. E. Eur. Phys. J. B 2015, 88, 248.
- (48) Hasan, M. T.; Gonzalez-Rodriguez, R.; Ryan, C.; Coffer, J. L.; Naumov, A. V. ACS Appl. Mater. Interfaces 2019, 11, 39035–39045.
- (49) Lyuleeva, A.; Helbich, T.; Rieger, B.; Lugli, P. J. Phys. D: Appl. Phys. 2017, 50, 135106.
- (50) Kharadi, M. A.; Malik, G.-F. A.; Shah, K. A.; Khanday, F. A. *Int. J. Numer. Model.* **2021**, 34, No. e2809.
- (51) Lu, F.; Yang, J.; Li, R.; Huo, N.; Li, Y.; Wei, Z.; Li, J. J. Mater. Chem. C 2015, 3, 1397–1402.
- (52) Qu, Y.; Wu, Z.; Ai, M.; Guo, D.; An, Y.; Yang, H.; Li, L.; Tang, W. J. Alloys Compd. **2016**, 680, 247–251.
- (53) Echtermeyer, T. J.; Britnell, L.; Jasnos, P. K.; Lombardo, A.; Gorbachev, R. V.; Grigorenko, A. N.; Geim, A. K.; Ferrari, A. C.; Novoselov, K. S. *Nat. Commun.* **2011**, *2*, 458.
- (54) Tang, L.; Ji, R.; Li, X.; Bai, G.; Liu, C. P.; Hao, J.; Lin, J.; Jiang, H.; Teng, K. S.; Yang, Z.; Lau, S. P. ACS Nano **2014**, *8*, 6312–6320.
- (55) Hu, P.; Zhang, J.; Yoon, M.; Qiao, X.-F.; Zhang, X.; Feng, W.; Tan, P.; Zheng, W.; Liu, J.; Wang, X.; Idrobo, J. C.; Geohegan, D. B.; Xiao, K. *Nano Res.* **2014**, *7*, 694–703.
- (56) Hu, P.; Wen, Z.; Wang, L.; Tan, P.; Xiao, K. ACS Nano 2012, 6, 5988-5994.
- (57) Hu, P.; Wang, L.; Yoon, M.; Zhang, J.; Feng, W.; Wang, X.; Wen, Z.; Idrobo, J. C.; Miyamoto, Y.; Geohegan, D. B.; Xiao, K. *Nano Lett.* **2013**, *13*, 1649–1654.
- (58) Li, Y.; Zheng, W.; Huang, F. PhotoniX 2020, 1, 15.
- (59) Tsai, D.-S.; Liu, K.-K.; Lien, D.-H.; Tsai, M.-L.; Kang, C.-F.; Lin, C.-A.; Li, L.-J.; He, J.-H. ACS Nano 2013, 7, 3905–3911.
- (60) Nayfeh, M. H.; Satish, R.; Nayfeh, O. M.; Smith, A.; Therrien, J. IEEE Trans. Nanotechnol. 2005, 4, 660–668.
- (61) Rasool, K.; Rafiq, M. A.; Ahmad, M.; Imran, Z.; Hasan, M. M. Appl. Phys. Lett. **2012**, 101, 253104.
- (62) Feng, B.; Zhu, J.; Xu, C.; Wan, J.; Gan, Z.; Lu, B.; Chen, Y. Nanoscale Res. Lett. **2019**, 14, 39.
- (63) Kim, J.; Joo, S. S.; Lee, K. W.; Kim, J. H.; Shin, D. H.; Kim, S.; Choi, S.-H. ACS Appl. Mater. Interfaces **2014**, *6*, 20880–20886.
- (64) Giannozzi, P.; Baroni, S.; Bonini, N.; Calandra, M.; Car, R.; Cavazzoni, C.; Ceresoli, D.; Chiarotti, G. L.; Cococcioni, M.; Dabo, I.; Dal Corso, A.; de Gironcoli, S.; Fabris, S.; Fratesi, G.; Gebauer, R.; Gerstmann, U.; Gougoussis, C.; Kokalj, A.; Lazzeri, M.; Martin-Samos, L.; Marzari, N.; Mauri, F.; Mazzarello, R.; Paolini, S.; Pasquarello, A.; Paulatto, L.; Sbraccia, C.; Scandolo, S.; Sclauzero, G.; Seitsonen, A. P.; Smogunov, A.; Umari, P.; Wentzcovitch, R. M. J. Phys.: Condens. Matter 2009, 21, No. 395502.
- (65) Perdew, J. P.; Burke, K.; Ernzerhof, M. Phys. Rev. Lett. 1996, 77, 3865–3868.
- (66) Grimme, S.; Antony, J.; Ehrlich, S.; Krieg, H. J. Chem. Phys. 2010, 132, 154104.

- (67) Monkhorst, H. J.; Pack, J. D. Phys. Rev. B 1976, 13, 5188-5192.
- (68) Blöchl, P. E. Phys. Rev. B 1994, 50, 17953-17979.

# Recommended by ACS

## **Ab Initio Computer Simulations on Interfacial** Properties of Single-Layer MoS<sub>2</sub> and Au Contacts for **Two-Dimensional Nanodevices**

Gabriele Boschetto, Aida Todri-Sanial, et al.

APRIL 28, 2022

ACS APPLIED NANO MATERIALS

READ 🗹

## **Toward Low-Temperature Solid-Source Synthesis of** Monolayer MoS<sub>2</sub>

Alvin Tang, Eric Pop, et al.

AUGUST 24, 2021

ACS APPLIED MATERIALS & INTERFACES

READ **'** 

## A Route to Obtaining Low-Defect III-V Epilayers on Si(100) Utilizing MOCVD

Manali Nandy, Thomas Hannappel, et al.

AUGUST 23, 2021

CRYSTAL GROWTH & DESIGN

READ 🗹

## Chemical Vapor Deposition of MoS<sub>2</sub> for Energy Harvesting: Evolution of the Interfacial Oxide Layer

Tim Verhagen, Otakar Frank, et al.

JUNE 10, 2020

ACS APPLIED NANO MATERIALS

READ 🗹

Get More Suggestions >